PCCP

ROYAL SOCIETY OF CHEMISTRY

PAPER

View Article Online
View Journal | View Issue

Cite this: *Phys. Chem. Chem. Phys.*, 2024, **26**, 12009

First-principles study of multifunctional Mn_2B_3 materials with high hardness and ferromagnetism†

Chunhong Xu, *[a] Kuo Bao,[b] Sheng Wang,[a] Gang Wu,[a] Shuailing Ma,[c] Liangliang Li,[a] Paul K. Chu[d] and Chao Liu *[a]

Received 12th September 2023,
Accepted 20th March 2024

DOI: 10.1039/d3cp04414a

rsc.li/pccp

Transition metal boride TM_2B_3 is widely studied in the field of physics and materials science. However, Mn_2B_3 has not been found in Mn–B systems so far. Mn_2B_3 undergoes phase transitions from *Cmcm* (0–28 GPa) to *C*2/*m* (28–80 GPa) and finally to *C*2/*c* (80–200 GPa) under pressure. Among these stable phases, *Cmcm*- and *C*2/*m*-Mn_2B_3s comprise six-membered boron rings and *C*2/*c*-Mn_2B_3 has wavy boron chains. They all have good mechanical properties and can become potential multifunctional materials. The strong B–B covalent bonding is mainly responsible for the structural stability and hardness. Comparison of the hardness of the five TM_2B_3s with different bonding strengths of TM–B and B–B bonds reveals a nonlinear change in the hardness. According to the Stoner model, these structures possess ferromagnetism, and the corresponding magnetic moments are almost the same as those of GGA and GGA + *U* (*U* = 3.9 eV, *J* = 1 eV).

Introduction

Functional materials, which can be categorized based on the mechanical, electrical, and magnetic functions, *etc.*, have drawn a lot of attention in materials science, engineering, and industrial applications. Multifunctional materials have two or more functions and transition metal borides (TMBs) are especially attractive. For example, ReB_2 and CrB_4 have metallic properties and superhardness,[1,2] FeB_4 has superconductivity and superhardness,[3,4] and WB_3 and MoB_3 have superhardness and anomalously low lattice thermal conductivity.[5,6] Transition metal borides are formed by inserting small, covalent boron atoms (B) into transition metals (TMs) with rich valence electrons, high bulk modulus, and high hardness.[7,8] Many more transition metal borides have been synthesized at ambient pressure than at high pressure or high temperature,[7,9] because of low production cost and wide applications. For example, arc melting and metathesis reactions have been used to synthesize OsB_2,[10] RuB_2,[11] ReB_2,[1,9,12,13] WB_4,[14,15] and CrB_4.[2] This family of interesting materials has attracted the attention of experimentalists and theorists[16–20] and ignited the interest in studying multifunctional transition metal borides.

Transition metal manganese (Mn) has many oxidation states (+2, +3, +4, +6, and +7) and a high capability of providing electrons. Boron atoms have the ability to form multipurpose frameworks. It combines with boron atoms to form many types of multifunctional materials such as Mn_4B, Mn_2B, FeB–MnB, Mn_3B_4, AlB_2–MnB_2, MnB_3, MnB_4, MnB_6, MnB_{12}, and MnB_{23}.[21,22] They are mostly used as corrosion resistant materials and the hardness is of great concern. Under a load of 0.98 N, AlB_2–MnB_2 has a low hardness of 7.5 GPa.[23] A theoretical study has revealed that ReB_2–MnB_2 is a potential superhard material with a theoretical hardness of 43.9 GPa.[24] Unfortunately, this structure has not been synthesized experimentally.[22,23,25,26] Niu *et al.* synthesized MnB_3 with a hardness of 32.3 GPa.[27] B-rich MnB_4 with a hardness of 34.6–37.8 GPa has been synthesized by different methods.[22,27–29]

Manganese is a spin-polarized atom and its borides generally exhibit interesting magnetic properties, for instance, ferromagnetic MnB,[30] AlB_2–MnB_2,[25] and Mn_3B_4[27] as well as ferromagnetic and paramagnetic MnB_4[28] (*e.g.* <150 K: ferromagnetic, 150–200 K: paramagnetic). There have been investigations on Mn–B compounds including two-dimensional Mn_2B_3,[31] while three-dimensional Mn_2B_3 has always been a mystery in theories and experiments so far. At the same time, research of three-dimensional TM_2B_3 compounds is flourishing, *e.g.* experimental V_2B_3,[32] Cr_2B_3,[33] Ru_2B_3[34] and Nb_2B_3[35] as well as theoretical Zr_2B_3,[36] and Ti_2B_3.[37]

Owing to the seemingly contradictory results, it is important to identify the pressure range for thermodynamically stable

[a] *School of Physics and Electronic Engineering, Northeast Petroleum University, Daqing, 163318, China. E-mail: xuchunhong@nepu.edu.cn, msm-liu@126.com*
[b] *State Key Laboratory of Superhard Materials, College of Physics, Jilin University, Changchun, 130012, People's Republic of China. E-mail: baokuo@jlu.edu.cn*
[c] *Institute of High Pressure Physics, School of Physical Scientific and Technology, Ningbo University, Ningbo, 315211, China. E-mail: msljlu@163.com*
[d] *Department of Physics, Department of Materials Science and Engineering, and Department of Biomedical Engineering, City University of Hong Kong, Tat Chee Avenue, Kowloon, Hong Kong, China*

† Electronic supplementary information (ESI) available. See DOI: https://doi.org/10.1039/d3cp04414a

Mn_2B_3 and the corresponding structures and properties. Herein, Mn_2B_3 is studied theoretically at 0–240 GPa. Two phase transitions occur at 28 GPa and 80 GPa and the structure of *Cmcm* is followed by *C*2/*m* and *C*2/*c*. The boron atoms form six-membered rings and wavy chains. Their mechanical, electronic, and magnetic properties are derived and discussed in this paper.

Computational details

Considering the variety of stoichiometries and structures of the Mn–B system, the variable-composition structure predictions method in USPEX[38,39] was performed firstly at 50, 100, and 200 GPa to confirm the existence of Mn_2B_3. Subsequently, the 1–4 formula units (f.u.) of Mn_2B_3 at 0, 50, 100 and 200 GPa were determined using the CALYPSO code based on the particle swarm optimization (PSO) algorithm.[40,41] Both of these two methods were very successful in predicting binary high-pressure crystalline structures.[42–45] For comprehensiveness, the structures of TM_2B_3s (TM = Ti, V(Cr, Nb), Zr and Ru) reported by both experiments and theories were considered and calculated by comparing the relative stability of Mn_2B_3. All the structures were relaxed using density-functional theory (DFT) calculation implemented in the VASP code.[46] The Perdew–Burke–Ernzerhof (PBE) functional and exchange correlation within GGA[47] were applied. The valence electron configurations for Ti, V, Cr, Mn, Zr, Nb, Ru and B were $3d^34s^1$, $3d^44s^1$, $3d^54s^1$, $3d^64s^1$, $4s^24p^64d^35s^1$, $4p^64d^45s^1$, $4d^75s^1$, and $2s^22p^1$. To ensure the convergence of enthalpy to less than 1 meV per atom, a plane-wave cutoff energy of 500 eV and dense *k*-point sampling with the grid spacing of $2\pi \times 0.03$ Å^{-1} were chosen. The denser *k*-point sampling of $2\pi \times 0.02$ Å^{-1} was set to calculate the electronic structure and bonding. The phonon dispersion curves were obtained by the supercell method.[48] The strain–stress method was employed to calculate the elastic constants, while the bulk modulus *B*, shear modulus *G*, Young's modulus *Y*, *B*/*G*, and Poisson's ratio ν were derived by Voigt–Reuss–Hill approximation.[49] The theoretical hardness was calculated based on Chen's model[50] and Gao's model.[51,52] The Mulliken bond population was calculated *via* the supercell method with the CASTEP code.[53,54] The ultra-soft Vanderbilt pseudopotential (USPP)[55] with PBE-GGA was chosen. The cutoff energy and *k*-mesh were the same as the setting in VASP calculations. The spin-polarization effects were considered in all the calculations. The crystal orbital Hamiltonian populations (COHPs) were calculated using the LOBSTER program.[56]

Results and discussion

The enthalpy results of the Mn–B system, which verify the existence of Mn_2B_3 are presented in Fig. S1 (ESI†). According to the calculated phase diagram in the past[27,57,58] and present, we can roughly identify Mn_2B, MnB, MnB_2, Mn_3B_4 and MnB_4. The existence of these stoichiometric manganese borides has been verified[27,57–59] and will not be considered here. Fig. S1c (ESI†) reveals that a new three-dimensional compound with a Mn to B ratio of 2 : 3 can be synthesized at 200 GPa. It has never been reported before both experimentally and theoretically so far. After searching and optimizing the competitive structures, the enthalpies with respect to α-Mn,[60] α-B (0–19 GPa), γ-B (19–89 GPa), and α-Ga-type B (89–130 GPa)[61] as a function of pressure are shown in Fig. 1. The pressure points where the phase transition occurs are separated by dotted lines. Two phase transitions are found for Mn_2B_3 between 0 and 240 GPa. At about 28 GPa, Mn_2B_3 has an orthorhombic structure with the space group *Cmcm*. The enthalpy of *Cmcm*-Mn_2B_3 is very close to that of the monoclinic *C*2/*m*-Mn_2B_3. *Cmcm*-Mn_2B_3 has a lower enthalpy at low pressure as shown in Fig. 1b, suggesting that it is the thermodynamic ground state. At above 28 GPa, Mn_2B_3 changes from *Cmcm* to *C*2/*m* up to 80 GPa, which is the first phase transition for Mn_2B_3. The *C*2/*c* phase is more favorable than the *C*2/*m* phase at the pressure range between 80 and 240 GPa. This is the second phase transition.

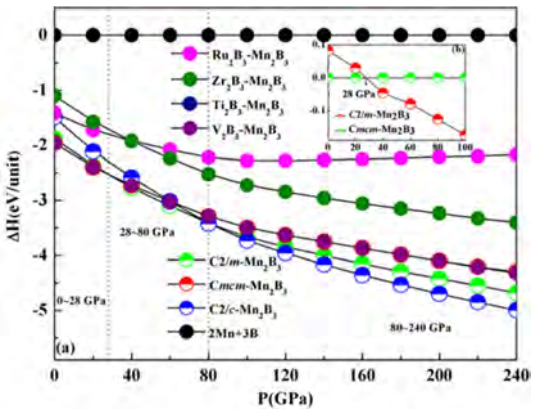

Fig. 1 (a) Formation enthalpies per formula unit of the various structures of Mn_2B_3 as a function of pressure; inset: (b) relative enthalpy of *C*2/*m*-Mn_2B_3 with respect to *Cmcm*-Mn_2B_3. Same horizontal and vertical coordinates of (a) and (b).

The optimized structural parameters at ambient pressure are listed in Tables S1–S3 (ESI†) and their atomic arrangements are shown in Fig. 2. For *Cmcm*-Mn_2B_3, its equilibrium lattices are a = 2.952 Å, b = 17.957 Å, and c = 2.965 Å, and both Mn and B atoms occupy the Wyckoff 4c site. These parameters are similar to those of the binary transition metal borides TM_2B_3, for example, Ti_2B_3, Nb_2B_3, V_2B_3 and Cr_2B_3 (Table S4, ESI†) belonging to the V_2B_3 family. As a V_2B_3-type structure, *Cmcm*-Mn_2B_3 consists of slabs along the *y* axis. A slab includes three layers of BMn_6 trigonal prisms (Fig. 2a) parallel to the *a* axis. The boron atoms form a triple chain sandwich between the four layers of manganese atoms along the *c* axis. These boron atoms remain to be the centre of each BMn_6 trigonal prism. Fig. 2b shows that the B(2) atom is closer to Mn(1) (2.165 Å) than Mn(2) (2.341 Å); Mn(2)–B(1), Mn(2)–B(3), and Mn(2)–B(1) have semblable distances of 2.277 Å, 2.259 Å, and 2.265 Å, respectively. The interatomic distance B(2)–B(3) (1.769 Å) is longer by 3% and 2.8% than B(1)–B(1) (1.717 Å) and B(2)–B(3) (1.720 Å) in the six-membered boron ring. *C*2/*m*-Mn_2B_3 has four molecules in one unit cell with the optimized lattice parameters of a = 7.554 Å, b = 2.953 Å, c = 8.114 Å, $\alpha = \gamma = 90^\circ$, and $\beta = 121.21^\circ$. It shows a sandwiched structure with bending layers of B atoms separated

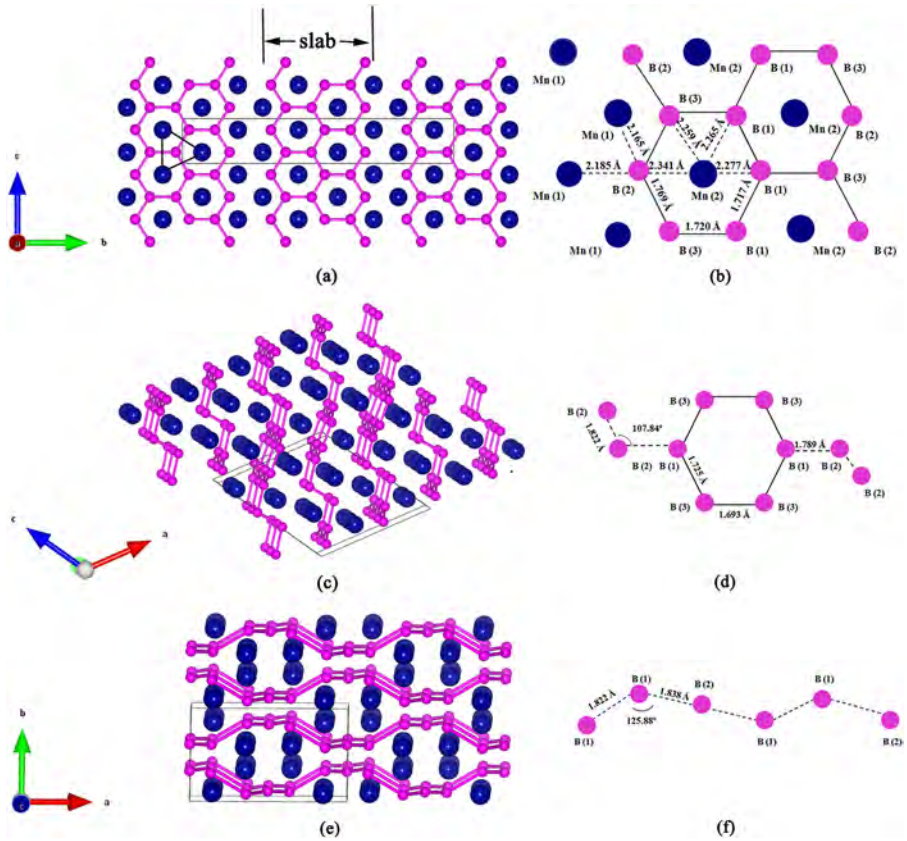

Fig. 2 Predicted structures of Mn_2B_3 and the corresponding boron arrangements. (a) and (b) *Cmcm*; (c) and (d) *C*2/*m*; (e) and (f) *C*2/*c*.

by layers of Mn atoms (Fig. 2c). Similarly, two B(1) and four B(3) atoms form a six-membered ring in this monoclinic structure (Fig. 2d). The bond lengths of B(1)–B(3) and B(3)–B(3) are 1.725 Å and 1.693 Å, respectively. Two longer B(2)–B(2) bonds (1.822 Å) in the bent position are connected with two B(1) atoms at an angle of 107.84°. The copular bond length (B(1)–B(2), 1.789 Å) is shorter than B(2)–B(2), suggesting stronger B–B interaction. The Mn–B bond lengths of *C*2/*m*-Mn_2B_3 range from 2.086 Å to 2.330 Å, similar to V_2B_3 (2.229–2.359 Å) and Cr_2B_3 (2.117–2.343 Å). The dense *C*2*c*-Mn_2B_3 structure also has four molecules per unit cell. The lattice parameters are a = 6.968 Å, b = 4.025 Å, c = 5.507 Å, $\alpha = \gamma = 90°$, and β = 103.27°. In this structure, the six-membered boron ring is broken and becomes wavy boron chains. Manganese atoms are situated between the wave peaks of the two adjacent chains (Fig. 2e). The basic unit of the wavy chain consists of two B(1) atoms and one B(2) atom. The bond lengths (B(1)–B(1), B(1)–B(2)) and bond angle are 1.822 Å, 1.838 Å, and 125.88° (Fig. 2f), respectively. These B–B bond lengths are similar to those of Nb_2B (1.809–1.843 Å).

Phonon frequencies are calculated for *Cmcm*-Mn_2B_3, *C*2/*m*-Mn_2B_3 and *C*2/*c*-Mn_2B_3 at different pressures to gauge the dynamic stability as shown in Fig. S2 (ESI†). When the low-frequency region shows imaginary frequencies, the structure is dynamically unstable. As shown in Fig. S2 (ESI†), there are no imaginary frequencies for all predicted structures throughout the Brillouin zone, suggesting good dynamical stability at high pressure and the ability of quenching at ambient pressure. According to the corresponding partial phonon density of states, it can be concluded that manganese atoms dominate the low-frequency region, while boron atoms govern the high-frequency region. Moreover, structural phase transformation can be seen from the soft modes in the phonon dispersion curves.[62] With increasing pressure, the soft phonon modes of *Cmcm*-Mn_2B, *C*2/*m*-Mn_2B_3, and *C*2/*c*-Mn_2B_3 along the S–U, A–E, and A–D appear and finally disappear (Fig. S2b and Fig. 2d, f). At 0 GPa, the optical modes in the three structures of Mn_2B_3 are doubly degenerate at the Γ point (Fig. S2a and Fig. 2c, e), indicating their metallic nature.

The mechanical properties are important to industrial applications. The elastic constants of TM_2B_3s (Mn_2B_3, Cr_2B_3, V_2B_3, Nb_2B_3 and Ti_2B_3) with the space group *Cmcm*, *C*2/*m*- and *C*2/*c*-Mn_2B_3 are shown in Table S5 (ESI†). With regard to Cr_2B_3, V_2B_3 and Nb_2B_3, there is no experimental data on the mechanical properties for reference, and so the calculated results only provide reasonable criteria to estimate the potential application of Mn_2B_3. According to the Born–Huang criterion,[63] these structures are mechanically stable at 0 GPa. The compressional constants C_{11}, C_{22}, and C_{33} are in line with the ability to resist deformation along the *a*-, *b*- and *c*-axes, respectively. The elastic constants and moduli of the five TM_2B_3s are shown in Fig. 3a. C_{22} and C_{33} in the different TM_2B_3s are nearly the same, and the C_{11} values are the smallest, suggesting high incompressibility along the *b*- and *c*-axes. Among these TM_2B_3s, Mn_2B_3 has lower incompressibility along the three axes due to the smaller C_{11},

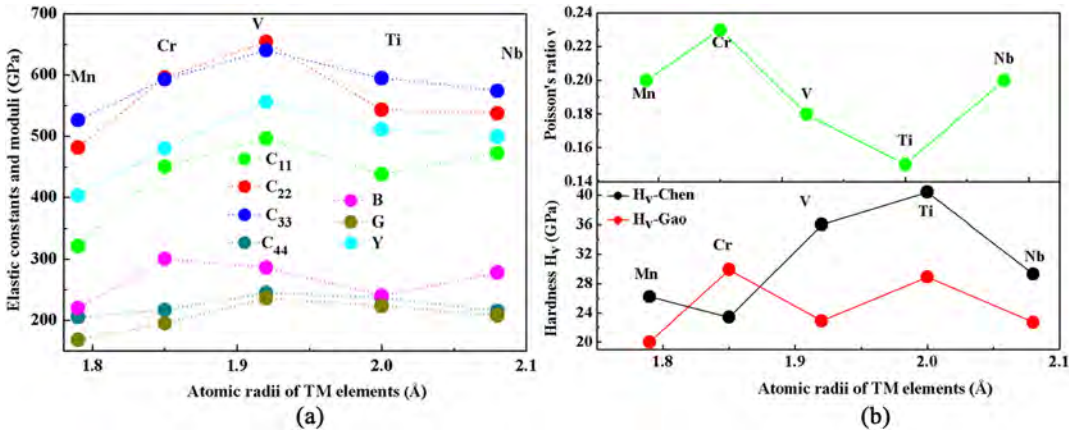

Fig. 3 (a) Elastic constants and moduli and (b) Poisson's ratio and hardness of the five TM_2B_3s (TM = Mn, Cr, V, Nb, and Ti).

C_{22} and C_{33} values. In comparison, $C2/m$- and $C2/c$-Mn_2B_3 show the largest C_{22} values implying high incompressibility along the b-axis. The shear constant C_{44} is a better predictor for the hardness. The similar C_{44} values of Mn_2B_3 (205 GPa) and Nb_2B_3 (215 GPa), which are smaller those of than V_2B_3 (245 GPa) and Ti_2B_3 (237 GPa), indicate similar hardness. $C2/m$- and $C2/c$-Mn_2B_3 (188 GPa and 151 GPa) have smaller 8.3% and 26.3% C_{44} than $Cmcm$-Mn_2B_3, revealing slightly smaller hardness. Based on the calculated elastic constants and Voiget–Reuss–Hill (VRH) approximation, the results of bulk modulus B, shear modulus G, Young's modulus Y, G/B, and Poisson's ratio ν are presented in Table 1 and Fig. 3. The B value of Mn_2B_3 (220 GPa) is smaller than those of the other four TM_2B_3s (above 240 GPa). However, the larger B values of $C2/m$- and $C2/c$-Mn_2B_3 (259 GPa and 297 GPa) suggest the better ability to resist volume deformation than $Cmcm$-Mn_2B_3. In general, the hardness is associated with G rather than B. The change of B and Y is the same as the shear constant C_{44} in the five TM_2B_3s, and the weakest ability of resisting shear, tension, and pressure deformation is observed from Mn_2B_3. Compared to $Cmcm$-Mn_2B_3 (168 GPa), $C2/m$- and $C2/c$-Mn_2B_3 have slightly lower G values (155 GPa and 127 GPa). The ν value of 0.2 for Mn_2B_3, between 0.23 for Cr_2B_3 and 0.18 for V_2B_3, implies some degree of covalent bonding. $C2/m$- and $C2/c$-Mn_2B_3 have a smaller degree of covalent bonding due to larger ν (0.25 and 0.31). All five TM_2B_3s and $C2/m$-Mn_2B_3 have larger G/B values than 0.571,[64] indicating a brittle nature. $C2/c$-Mn_2B_3 is a ductile material due to the smaller B/G of 0.429. The slightly large C_{44} and G, large G/B, and low ν of $Cmcm$- and $C2/m$-Mn_2B_3 indicate that they are potentially hard materials. On the contrary, $C2/c$-Mn_2B is a soft material. Hard materials are usually used in cutting tools and hard coatings. We used Chen's[50] and Gao's[16,51] models to calculate hardness. The two models have achieved great success in calculating hardness both experimentally and theoretically. According to Chen's equation of Vickers hardness: $H_\nu = 2(k^2G)^{0.585} - 3$ ($k = G/B$), the calculated results verify that $Cmcm$- and $C2/m$-Mn_2B_3 are hard materials, since their Vickers hardness values are 26.2 GPa and 18.0 GPa, respectively. However, $C2/c$-Mn_2B_3 has a soft nature with a Vickers hardness of 9.6 GPa. A hard–soft transition exists in the three Mn_2B_3 phases. The results of Gao's model are found in Tables S6–S12 (ESI†), indicating that all phases of Mn_2B_3 belong to hard materials. $Cmcm$- and $C2/c$-Mn_2B_3 have weakly covalent Mn–Mn bonds (Tables S1 and S12, ESI†); however, $C2/m$-Mn_2B_3 has no such bond (Table S11, ESI†).

Fig. 3b shows that the hardness values of the five TM_2B_3s exhibit no linear change with increasing atomic radii of the transition metal TM elements. The trend of change is the same except for Cr_2B_3. The Bader charges[65] and bonding strength of the five TM_2B_3s as well as $C2/m$ and $C2/c$-Mn_2B_3 are studied. The calculated results are presented in Tables S13 and S14 (ESI†). The integrated crystal orbital Hamiltonian population (ICOHP) values can be used as an indicator of the bonding strength.[66] A negative ICOHP value indicates bonding and a positive value indicates antibonding. In the present study, we only emphasize the stronger TM–B and B–B bonding and

Table 1 Bulk modulus B (GPa), shear modulus G (GPa), Young's modulus Y (GPa), G/B, Poisson's ratio ν and Vickers hardness (GPa) of V_2B_3-type structures, $C2/m$-Mn_2B_3 and $C2/c$-Mn_2B_3

Phase (SG)	Mn_2B_3 ($Cmcm$)	Cr_2B_3 ($Cmcm$)	V_2B_3 ($Cmcm$)	Nb_2B_3 ($Cmcm$)	Ti_2B_3 ($Cmcm$)	Mn_2B_3 ($C2/m$)	Mn_2B_3 ($C2/c$)
B	220	300	286	278	240	259	297
G	168	195	236	208	223	155	127
Y	403	480	556	499	511	387	334
G/B	0.769	0.649	0.833	0.752	0.926	0.599	0.429
ν	0.20	0.23	0.18	0.20	0.15	0.25	0.31
H_v-Chen	26.2	23.4	36.0	29.3	40.4	18.0	9.6
H_v-Gao	20.0	29.9	22.9	22.7	28.9	20.9	15.6

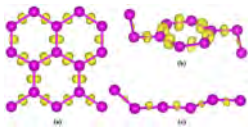

Fig. 4 ELFs of (a) *Cmcm*-Mn_2B_3, (b) *C*2/*m*-Mn_2B_3 and (c) *C*2/*c*-Mn_2B_3. The ELF isosurface value is 0.5.

average ICOHP values. As shown in Table S14 (ESI†), the B–B bonding is obviously stronger than TM–B bonding due to the larger average ICOHP. Hence, it is believed that strong B–B bonding plays a dominant role in the hardness. The electron localization functions (ELFs) of the three Mn_2B_3 phases are computed and shown in Fig. 4. The high electron localization in the region between the B atoms indicates strong covalent B–B bonding. According to the −ICOHP values (Table S14, ESI†), Cr_2B_3 has the highest hardness due to the strongest strength of the TM–B and B–B bonds in Gao's model. According to the −ICOHP values (Table S14, ESI†), the bonding strength of the Mn–B and B–B bonds successively decreases in *Cmcm*-, *C*2/*m*- and *C*2/*c*-Mn_2B, which is a good match for changes of their hardness in Chen's model. Furthermore, Mn_2B_3 has higher hardness with the six-membered B ring (Fig. 4a and b) compared to the wavy chain (Fig. 4c). In other words, differences in hardness mainly come from different bond strengths (TM–B and B–B bonds).

The energy *versus* volume curves for the three phases of Mn_2B_3 with non-spin-polarized and spin-polarized effects are calculated. Fig. 5(a), (c) and (e) show that *Cmcm*-, *C*2/*m*-, and *C*2/*c*-Mn_2B_3 are spin-polarized materials. In particular, the spin-polarized states of the three phases of Mn_2B_3 are more stable than those of the non-spin-polarized states at high pressure. Fig. 5(b), (d) and (f) show the sum of the spin-polarized up and down density of states (DOSs). They are characteristic of metals due to the emergence of DOS at the Fermi energy levels.

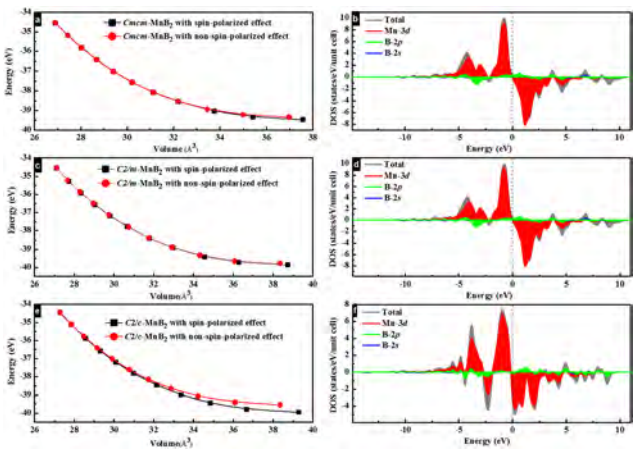

Fig. 5 Energy–volume curves of (a) *Cmcm*-Mn_2B_3, (c) *C*2/*m*-Mn_2B_3, and (e) *C*2/*c*-Mn_2B_3 by considering the non-spin-polarized and spin-polarized effects. The corresponding DOSs (sum of spin-polarized up and down density of states) are shown in (b), (d), and (f), respectively. The vertical dashed line at zero is the Fermi energy level.

Moreover, there is spontaneous magnetization since the DOS in the three phases of Mn_2B_3 is nonzero, consequently leading to localized magnetic moments on the atoms. The Stoner model provides a quantitative criterion for spontaneous magnetization, which requires $N_{TM}(E_F) \times I_{TM} > 1$, where $N_{TM}(E_F)$ is the non-polarized partial density of states of the transition metal atom at the Fermi energy level and I_{TM} is the exchange–correlation integral.[67] The values of $N_{TM}(E_F) \times I_{TM}$ for *Cmcm*-, *C*2/*m*- and *C*2/*c*-Mn_2B_3s are 9.26, 6.36, and 7.40, respectively, and are larger than 1 indicating the ferromagnetic nature. The ferromagnetic moments mainly come from the Mn-3d states, and the B-2p states give rise to small negative magnetic moments. The magnetic moments of Mn_2B_3s are calculated to be 1.79, 1.09, and 1.29μ_B/Mn, respectively. Considering the on-site coulombic interactions of the Mn-3d electrons, GGA + *U* calculations are performed. Using U = 3.9 eV and J = 1 eV,[23] similar magnetic moments (1.75, 1.08 and 1.29μ_B/Mn) are obtained. As for *C*2/*m*- and *C*2/*c*-Mn_2B_3s, there is scarcely any difference in the magnetic moments between the GGA and GGA + *U* calculations. Combining a relatively high hardness and ferromagnetism makes Mn_2B_3s multifunctional materials. The results also widen our search for novel and applied materials. The B-2p and 2s states are in the energy range of −15 eV to −7.5 eV, suggesting strong covalent interactions between B atoms in accordance with the results of ELF being the key to the structural stability and hardness of Mn_2B_3s.

Conclusions

Mn_2B_3 falls on a convex hull at 200 GPa according to variable-composition structure predictions. Analysis of the evolution of the structure reveals that Mn_2B_3 undergoes *Cmcm*, *C*2/*m* and *C*2/*c* phase transformations. The calculated phonon curves and elastic constants verify the dynamics and stability at ambient pressure. Boron atoms form six-membered rings (*Cmcm* and *C*2/*m*) and wavy chains (*C*2/*c*) in these structures. Analysis of the chemical bonding indicates that strong covalent B–B and TM–B bonding mainly contributes to the structural stability and hardness, and causes the nonlinear variation of the hardness of the five TM_2B_3 compounds simultaneously. Our results on the electronic properties disclose the ferromagnetic stability. The magnetic moments of *Cmcm*-, *C*2/*m*-, and *C*2/*c*-Mn_2B_3 are 1.79 (1.75), 1.09 (1.08), and 1.29 (1.29) μ_B/Mn based on the GGA (GGA + *U*) calculations, respectively. These results demonstrate that Mn_2B_3 is indeed a multifunctional material, and future experimental efforts will be expected to synthesize this potentially multifunctional material.

Conflicts of interest

There are no conflicts to declare.

Acknowledgements

This work was supported by the Young Science Foundation of Northeast Petroleum University (2018QNL-37), Heilongjiang

Provincial Natural Science Foundation of China (JQ2023F001), Outstanding young and middle-aged research and innovation team of Northeast Petroleum University (KYCXTD201801), Local Universities Reformation and Development Personnel Training, Postdoctoral Scientific Research Development Fund of Heilongjiang Province (LBH-Q20081), the Central Support Fund for the Reform and Development of Local Universities, China (2023JCYJ-02), City University of Hong Kong Strategic Research Grant (SRG 7005505), and City University of Hong Kong Donation Research Grant (DON-RMG 9229021 and 9220061).

References

1 J. B. Levine, J. B. Betts, J. D. Garrett, S. Q. Guo, J. T. Eng, A. Migliori and R. B. Kaner, *Acta Mater.*, 2010, **58**, 1530–1535.
2 A. Knappschneider, C. Litterscheid, D. Dzivenko, J. A. Kurzman, R. Seshadri, N. Wagner, J. Beck, R. Riedel and B. Albert, *Inorg. Chem.*, 2013, **52**, 540–542.
3 A. N. Kolmogorov, S. Shah, E. R. Margine, A. F. Bialon, T. Hammerschmidt and R. Drautz, *Phys. Rev. Lett.*, 2010, **105**, 217003.
4 H. Y. Gou, N. Dubrovinskaia, E. Bykova, A. A. Tsirlin, D. Kasinathan, W. Schnelle, A. Richter, M. Merlini, M. Hanfland and A. M. Abakumov, *Phys. Rev. Lett.*, 2013, **111**, 157002.
5 Y. C. Liang, X. Yuan and W. Q. Zhang, *Phys. Rev. B: Condens. Matter Mater. Phys.*, 2011, **83**, 220102.
6 Y. C. Liang, J. Yang, X. Yuan, W. J. Qiu, Z. Zhong, J. H. Yang and W. Q. Zhang, *Sci. Rep.*, 2014, **4**, 5063.
7 R. B. Kaner, J. J. Gilman and S. H. Tolbert, *Science*, 2005, **308**, 1268.
8 R. W. Cumberland, M. B. Weinberger, J. J. Gilman, S. M. Clark, S. H. Tolbert and R. B. Kaner, *J. Am. Chem. Soc.*, 2005, **36**, 7264.
9 J. B. Levine, S. H. Tolbert and R. B. Kaner, *Adv. Funct. Mater.*, 2010, **19**, 3519–3533.
10 H. Y. Chung, J. Yang, S. H. Tolbert and R. B. Kaner, *J. Mater. Res.*, 2008, **23**, 1797–1801.
11 H. Y. Chung, M. B. Weinberger, J. M. Yang, S. H. Tolbert and R. B. Kaner, *Appl. Phys. Lett.*, 2008, **92**, 261904.
12 S. N. Tkachev, J. B. Levine, K. Alexer, A. P. Sokolov, S. Guo, J. T. Eng and R. B. Kaner, *Adv. Mater.*, 2010, **21**, 4284–4286.
13 Y. Suzuki, J. B. Levine, A. Migliori, J. D. Garrett, R. B. Kaner, V. R. Fanelli and J. B. Betts, *J. Acoust. Soc. Am.*, 2010, **127**, 2797–2801.
14 R. Mohammadi, A. T. Lech, M. Xie, B. E. Weaver, M. T. Yeung, S. H. Tolbert and R. B. Kaner, *Proc. Natl. Acad. Sci. U. S. A.*, 2011, **108**, 10958.
15 C. J. Liu, F. Peng, N. Tan, J. Liu, F. J. Li, J. Q. Qin, J. H. Wang, Q. M. Wang and D. W. He, *High Pressure Res.*, 2011, **31**, 275–282.
16 M. M. Zhong, X. Y. Kuang, Z. H. Wang, P. Shao, L. P. Ding and X. F. Huang, *J. Phys. Chem. C*, 2013, **117**, 10643–10652.
17 X. Z. Zhang, E. J. Zhao, Z. J. Wu, K. Li and Q. Y. Hou, *Comp. Mater. Sci.*, 2014, **95**, 377–383.
18 M. Maździarz and T. Mościcki, *J. Alloys Compd.*, 2016, **657**, 878–888.
19 H. Y. Gou, Z. P. Li, L. M. Wang, J. Lian and Y. C. Wang, *AIP Adv.*, 2012, **2**, 231.
20 Y. Pan, W. T. Zheng, W. M. Guan, K. H. Zhang and X. F. Fan, *J. Solid State Chem.*, 2013, **207**, 29–34.
21 A. Cely, L. E. Tergenius and T. Lundstrom, *J. Less-Common Met.*, 1978, **61**, 193–198.
22 X. X. Meng, K. Bao, P. W. Zhu, Z. He, Q. Tao, J. J. Li, Z. P. Mao and T. Cui, *J. Appl. Phys.*, 2012, **111**, 112616.
23 H. Y. Gou, G. Steinleneumann, E. Bykova, Y. Nakajima, N. Miyajima, Y. Li, S. V. Ovsyannikov, L. S. Dubrovinsky and N. Dubrovinskaia, *Appl. Phys. Lett.*, 2013, **102**, 061906.
24 S. Aydin and M. Simsek, *Phys. Rev. B: Condens. Matter Mater. Phys.*, 2009, **80**, 134107.
25 S. L. Ma, K. Bao, T. Qiang, C. H. Xu, X. K. Feng, P. W. Zhu and T. Cui, *Inorg. Chem.*, 2016, **55**, 11140–11146.
26 S. Khmelevskyi and P. Mohn, *J. Phys.: Condens. Matter*, 2012, **24**, 016001.
27 H. Y. Niu, X. Q. Chen, W. J. Ren, Q. Zhu, A. R. Oganov, D. Z. Li and Y. Y. Li, *Phys. Chem. Chem. Phys.*, 2014, **16**, 15866.
28 H. Y. Gou, A. A. Tsirlin, E. Bykova, A. M. Abakumov, G. V. Tendeloo, A. Richter, S. V. Ovsyannikov, A. V. Kurnosov, D. M. Trots, Z. Konôpková, H.-P. Liermann, L. Dubrovinsky and N. Dubrovinskaia, *Phys. Rev. B: Condens. Matter Mater. Phys.*, 2013, **89**, 064108.
29 A. Knappschneider, C. Litterscheid, N. C. George, J. Brgoch, N. Wagner, J. Beck, J. A. Kurzman, R. Seshadri and B. Albert, *Angew. Chem.*, 2014, **53**, 1684–1688.
30 S. L. Ma, K. Bao, Q. Tao, P. W. Zhu, T. Ma, B. Liu, Y. Z. Liu and T. Cui, *Sci. Rep.*, 2017, **7**, 43759.
31 Y. Sun, L. Wang, X. Li, X. Yao, X. Xu, T. Guo, A. He, B. Wang, Y. Liu and X. Zhang, *Appl. Phys. Lett.*, 2022, **121**, 183103.
32 Y. Yu, L. E. Tergenius, T. Lundström and S. Okada, *J. Alloys Compd.*, 1995, **221**, 86–90.
33 S. Okada, T. Atoda and I. Higashi, *J. Solid State Chem.*, 1987, **68**, 61–67.
34 M. Frotscher, A. Senyshyn and B. Albert, *Z. Anorg. Allg. Chem.*, 2012, **638**, 2078–2080.
35 S. Okada, K. Hamano, T. Lundström and I. Higashi, *AIP Conf. Proc.*, 1991, **231**, 456–459.
36 J. Li and C. Fan, *Phys. Chem. Chem. Phys.*, 2015, **17**, 1180–1188.
37 P. F. Li, R. L. Zhou and C. Z. Xiao, *ACS Appl. Mater. Interfaces*, 2015, **7**, 15607.
38 A. R. Oganov, A. O. Lyakhov and M. Valle, *Acc. Chem. Res.*, 2011, **44**, 227–237.
39 A. O. Lyakhov, A. R. Oganov, H. T. Stokes and Q. Zhu, *Comput. Phys. Commun.*, 2013, **184**, 1172–1182.
40 Y. C. Wang, J. Lv, L. Zhu and Y. M. Ma, *Phys. Rev. B: Condens. Matter Mater. Phys.*, 2010, **82**, 094116.
41 Y. C. Wang, J. Lv, L. Zhu and Y. M. Ma, *Comput. Phys. Commun.*, 2012, **183**, 2063–2070.
42 W. Chen, D. V. Semenok, A. G. Kvashnin, X. Huang, I. A. Kruglov, M. Galasso, H. Song, D. Duan, A. F. Goncharov and V. B. Prakapenka, *Nat. Commun.*, 2021, **12**, 273.

43 H. Niu, X.-Q. Chen, W. Ren, Q. Zhu, A. R. Oganov, D. Li and Y. Li, *Phys. Chem. Chem. Phys.*, 2014, **16**, 15866–15873.
44 L. Ma, K. Wang, Y. Xie, X. Yang, Y. Wang, M. Zhou, H. Liu, X. Yu, Y. Zhao and H. Wang, *Phys. Rev. Lett.*, 2022, **128**, 167001.
45 L. Zhang, Y. Wang, J. Lv and Y. Ma, *Nat. Rev. Mater.*, 2017, **2**, 1–16.
46 G. Kresse and J. Furthmüller, *Phys. Rev. B: Condens. Matter Mater. Phys.*, 1996, **54**, 11169.
47 J. P. Perdew, K. Burke and M. Ernzerhof, Generalized Gradient Approximation Made Simple, *Phys. Rev. Lett.*, 1996, **77**, 3865–3868.
48 A. Togo, F. Oba and I. Tanaka, *Phys. Rev. B: Condens. Matter Mater. Phys.*, 2008, **78**, 134106.
49 R. Hill, *Proc. Phys. Soc., London, Sect. A*, 1952, **65**, 349–354.
50 X. Q. Chen, H. Y. Niu, D. Z. Li and Y. Y. Li, *Intermetallics*, 2011, **19**, 1275–1281.
51 F. Gao, J. He, E. Wu, S. Liu, D. Yu, D. Li, S. Zhang and Y. Tian, *Phys. Rev. Lett.*, 2003, **91**, 015502.
52 M.-M. Zhong, X.-Y. Kuang, Z.-H. Wang, P. Shao, L.-P. Ding and X.-F. Huang, *J. Phys. Chem. C*, 2013, **117**, 10643–10652.
53 M. D. Segall, R. Shah, C. J. Pickard and M. C. Payne, *Phys. Rev. B: Condens. Matter Mater. Phys.*, 1996, **54**, 16317.
54 M. Segall, P. J. Lindan, M. A. Probert, C. J. Pickard, P. J. Hasnip, S. Clark and M. Payne, *J. Phys.: Condens. Matter*, 2002, **14**, 2717.
55 D. Vanderbilt, *Phys. Rev. B: Condens. Matter Mater. Phys.*, 1990, **41**, 7892.
56 V. L. Deringer, A. L. Tchougréeff and R. Dronskowski, *J. Phys. Chem. A*, 2011, **115**, 5461–5466.
57 B. Wang, X. Li, Y. X. Wang and Y. F. Tu, *J. Phys. Chem. C*, 2011, **115**, 21429–21435.
58 C. H. Xu, K. Bao, S. L. Ma, Y. B. Ma, S. L. Wei, Z. J. Shao, X. H. Xiao, X. K. Feng and T. Cui, *RSC Adv.*, 2017, **7**, 10559–10563.
59 H. Okamoto, *J. Phase Equilib.*, 1993, **14**, 121–122.
60 A. C. Lawson, A. C. Larson, M. C. Aronson, S. Johnson, Z. Fisk, P. C. Canfield, J. D. Thompson and R. B. V. Dreele, *J. Appl. Phys.*, 1994, **76**, 7049–7051.
61 A. R. Oganov, J. H. Chen, C. Gatti, Y. Z. Ma, Y. M. Ma, C. W. Glass, Z. X. Liu, T. Yu, O. O. Kurakevych and V. L. Solozhenko, *Nature*, 2009, **457**, 863–867.
62 H. R. Soni, S. K. Gupta and P. K. Jha, *Physica B*, 2011, **406**, 3556–3561.
63 M. Born and K. Huang, *Dynamical Theory of Crystal Lattices*, Oxford University Press, Oxford, 1954.
64 Z. J. Wu, E. J. Zhao, H. P. Xiang, X. F. Hao, X. J. Liu and J. Meng, *Phys. Rev. B: Condens. Matter Mater. Phys.*, 2007, **76**, 054115.
65 R. F. W. Bader and C. F. Matta, *J. Phys. Chem. A*, 2004, **108**, 8385–8394.
66 S. Maintz, V. L. Deringer, A. L. Tchougréeff and R. Dronskowski, *J. Comput. Chem.*, 2013, **34**, 2557–2567.
67 J. F. Janak, *Phys. Rev. B: Solid State*, 1977, **16**, 255–262.

Electronic Supplementary Material (ESI) for Physical Chemistry Chemical Physics.

Figure S1. The enthalpies of formation predicted by variable-composition evolutionary computations for the Mn–B system at (a) 50 GPa, (b) 100 GPa and (c) 200 GPa. Every circle represents an individual structure and the most stable ground-state phases (black circles) are connected to form the convex hull.

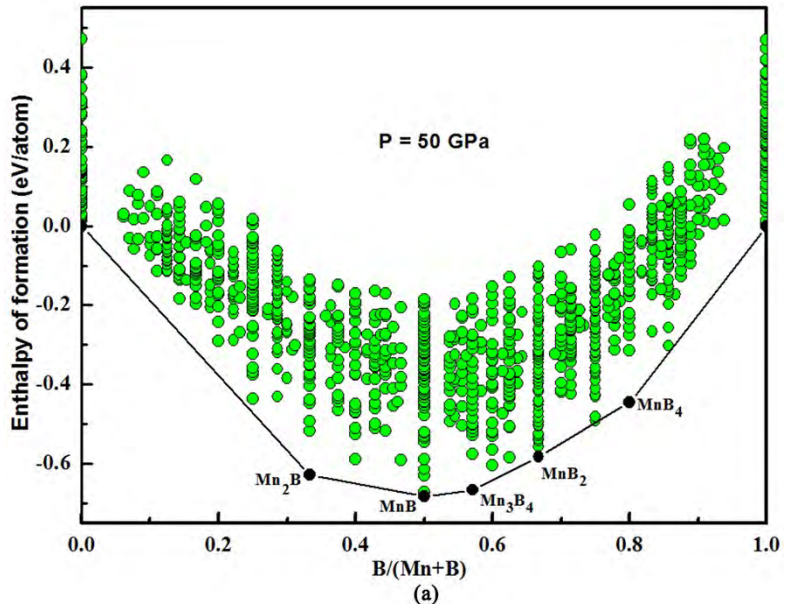

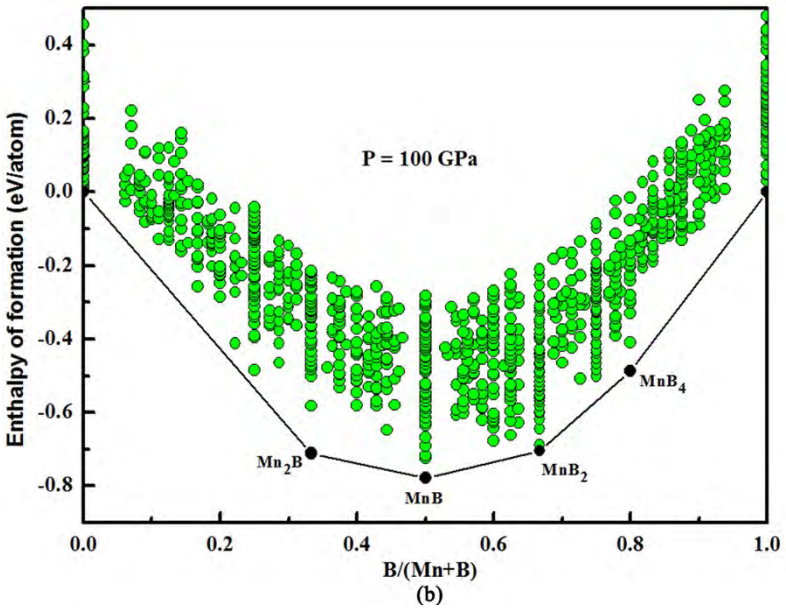

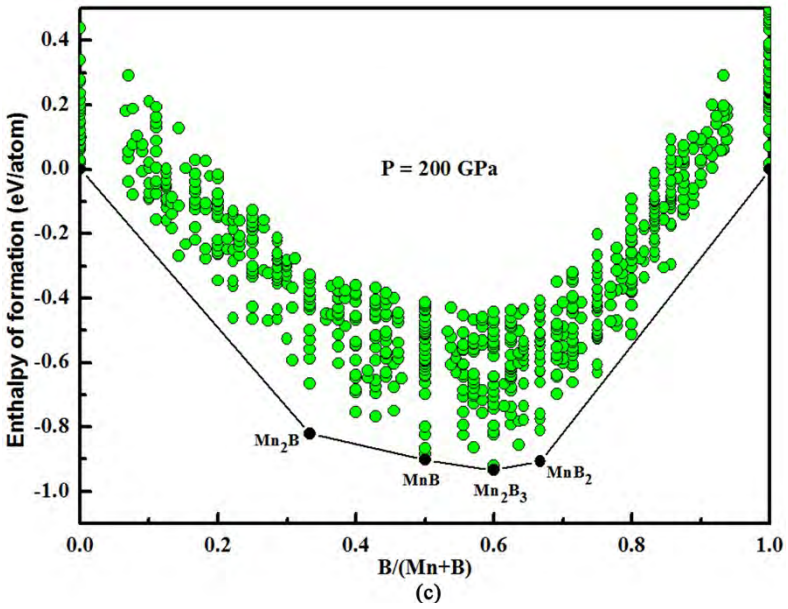

Table S1. Lattices Parameters and atomic coordinates of *Cmcm*-Mn_2B_3 at ambient pressure.

	Lattices Parameters (Å)	Atoms	x	y	z
	a = 2.952	Mn (4c)	0.00000	0.20468	0.75000
Cmcm-Mn_2B_3	b = 17.957	Mn (4c)	0.00000	0.07245	1.25000
	c = 2.965	B (4c)	0.50000	0.97591	1.25000
P = 0 GPa	α = β = γ = 90º	B (4c)	0.50000	0.17365	1.25000
		B (4c)	0.50000	0.88011	1.25000

Table S2. Lattices Parameters and atomic coordinates of *C*2/*m*-Mn_2B_3 at ambient pressure.

	Lattices Parameters (Å)	Atoms	x	y	z
	a = 7.554	Mn (4i)	0.05607	0.50000	0.85428
C2/m-Mn_2B_3	b = 2.953	Mn (4i)	0.20309	0.50000	0.61177
	c = 8.114	B (4i)	0.25716	0.50000	0.18584
P = 0 GPa	α =γ = 90º	B (4i)	0.48782	0.50000	0.60603
	β =121.107º	B (4i)	0.12637	0.00000	0.08799

Table S3. Lattices Parameters and atomic coordinates of *C*2/*c*-Mn_2B_3 at ambient pressure.

	Lattices Parameters (Å)	Atoms	x	y	z
	a = 6.968	Mn (8f)	0.35295	0.36384	0.35411
C2/c-Mn_2B_3	b = 4.025				
	c = 5.507	B (8f)	0.13691	0.36249	0.00206
P = 0 GPa	α =γ = 90º				
	β =150.324º	B (4e)	0.00000	0.65684	0.75000

Table S4. Unit cell parameters of binary borides Ti_2B_3, Mn_2B_3, Nb_2B_3, V_2B_3 and Cr_2B_3.

Phase	a (Å)	b (Å)	c (Å)	V (Å^3)
Mn_2B_3	2.952	17.957	2.965	157.216
Cr_2B_3	2.930	18.170	2.949	156.977
	3.027[a]	19.119[a]	2.954[a]	162.016[a]
V_2B_3	3.034	18.408	2.979	166.325
	3.061[b]	18.400[b]	2.984[b]	168.066[b]
Nb_2B_3	3.324	19.603	3.141	204.711
	3.306[c]	19.481[c]	3.129c[b]	201.528[c]
Ti_2B_3	3.243	19.024	3.038	187.422
	3.243[d]	19.025[d]	3.038[d]	187.431[d]

Ref a: Okada S.; Atoda T.; Higashi I. Structural investigation of Cr_2B_3, Cr_3B_4, and CrB by single-crystal diffractometry. *J. Solid State Chem*. **1987**, *68*, 61-67.

Ref b: Spear, K. E, Gilles, P. W. Phase and structure relationships in the vanadium-boron system. *HIGH TEMP SCI*. **1969**, *1*, 86-97.

Ref c: Yu, Y.; Tergenius, L. E.; Lundström, T.;Okada, S., A structural investigation of V_2B_3 by single-crystal diffractometry. *J. Alloys Compd.* **1995,** *221*, 86-90.

Ref d: Li, P. F.; Zhou, R. L.;Xiao, C. Z., Computational Analysis of Stable Hard Structures in the Ti–B System, *ACS Appl. Mater. Interfaces.* **2015,** *7*, 15607.

Figure S2. Phonon dispersion curves and phonon density of states for *Cmcm*-Mn_2B_3, at (a) 0 GPa. *C*2/*m*-Mn_2B_3, at (b) 0 GPa and (c) 80 GPa. *C*2/*c*-Mn_2B_3, at (d) 0 GPa and (e) 200 GPa.

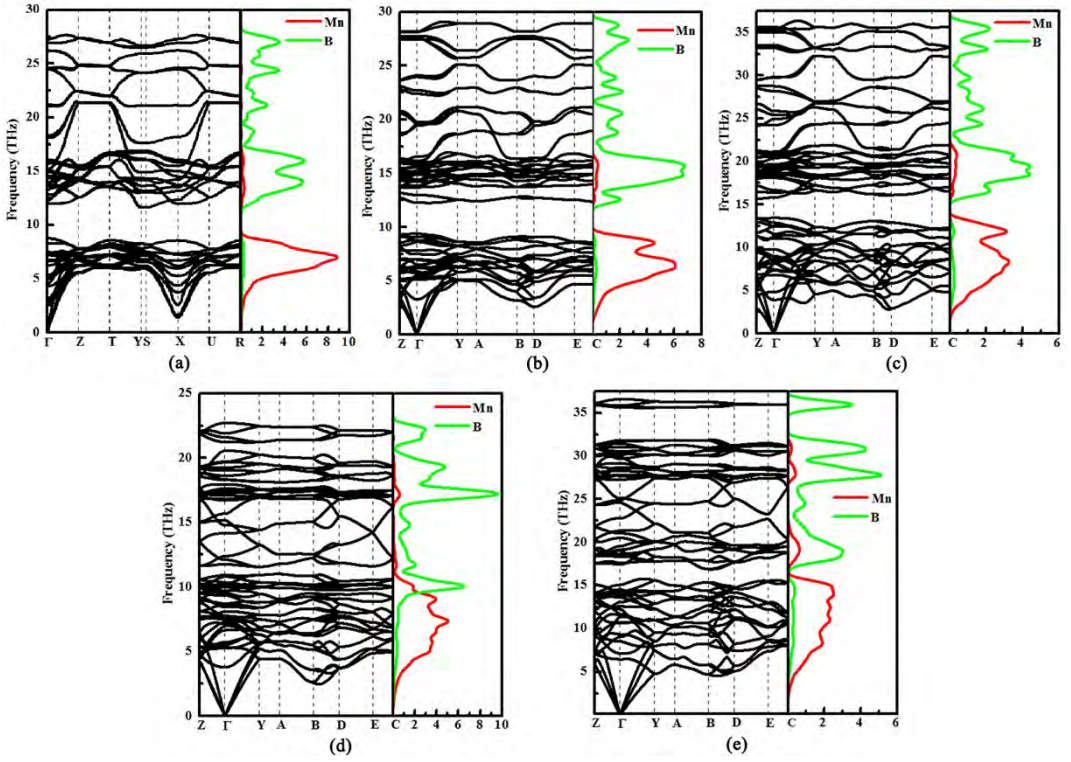

Table S5. Elastic constants of TM_2B_3s (SG: *Cmcm*) including Mn_2B_3, Cr_2B_3, V_2B_3, Nb_2B_3, and Ti_2B_3, as well as *C*2/*m*- and *C*2/*c*-Mn_2B_3 at ambient pressure.

Phase (SG)	C_{11}	C_{22}	C_{33}	C_{44}	C_{55}	C_{66}	C_{12}	C_{13}	C_{15}	C_{23}	C_{25}	C_{35}	C_{46}
Mn_2B_3 (*Cmcm*)	321	481	526	205	172	155	101	125		127			
Cr_2B_3 (*Cmcm*)	450	596	593	217	219	182	178	191		169			
V_2B_3 (*Cmcm*)	496	654	640	245	255	224	138	148		112			
Nb_2B_3 (*Cmcm*)	472	537	574	215	236	223	172	159		129			
Ti_2B_3 (*Cmcm*)	438	543	595	237	244	218	119	108		70			
Mn_2B_3 (*C*2/*m*)	430	494	430	188	155	172	127	194	24	179	-10	63	17
Mn_2B_3 (*C*2/*c*)	439	478	448	151	190	93	227	230	-23	199	38	-17	25

Table S6 Calculated bond parameters and Vickers hardness of Mn_2B_3(SG:*Cmcm*).

Bond type	d^{μ} (Å)	$v_b{}^{\mu}$ (Å^3)	*P*	f_m ($\times 10^{-3}$)	H_v (GPa)
B-B	1.709	0.661	0.98	0	20.0
	1.719	0.673	0.95	0	
	1.798	0.770	0.81	0	
	2.952	3.409	0.06	0	
	2.952	3.409	0.04	0	
Mn-B	2.061	1.160	0.04	5.940	
	2.134	1.288	0.26	5.940	
	2.235	1.479	0.34	5.940	
	2.261	1.532	0.05	5.940	
	2.261	1.532	0.09	5.940	
	2.263	1.536	0.05	5.940	
	2.386	1.800	0.05	5.940	
Mn-Mn	2.952	3.409	0.03	5.940	
	2.965	3.454	0.09	5.940	

Table S7 Calculated bond parameters and Vickers hardness of Cr_2B_3(SG:*Cmcm*).

Bond type	d^{μ} (Å)	v_b^{μ} (Å^3)	P	f_m ($\times 10^{-3}$)	H_v (GPa)
B-B	1.707	0.634	0.88	0	29.9
	1.729	0.659	0.82	0	
	1.766	0.702	0.76	0	
	2.930	3.208	0.05	0	
	2.930	3.208	0.02	0	
	2.930	3.208	0.03	0	
Cr-B	2.119	1.214	0.02	2.314	
	2.152	1.271	0.21	2.314	
	2.247	1.447	0.07	2.314	
	2.255	1.462	0.05	2.314	
	2.264	1.480	0.25	2.314	
	2.270	1.492	0.02	2.314	
	2.342	1.638	0.04	2.314	
Cr-Cr	2.930	3.208	0.07	2.314	
	2.949	3.271	0.02	2.314	

Table S8 Calculated bond parameters and Vickers hardness of V_2B_3(SG:*Cmcm*).

Bond type	d^{μ} (Å)	v_b^{μ} (Å^3)	P	f_m ($\times 10^{-3}$)	H_v (GPa)
B-B	1.724	0.893	0.89	0	22.9
	1.729	0.901	0.85	0	
	1.760	0.950	0.82	0	
V-B	2.230	1.932	0.18	1.542	
	2.293	2.101	0.04	1.542	
	2.296	2.109	0.06	1.542	
	2.300	2.120	0.01	1.542	
	2.330	2.204	0.24	1.542	
	2.358	2.285	0.05	1.542	
V-V	2.979	4.607	0.08	1.542	

Table S9 Calculated bond parameters and Vickers hardness of Nb_2B_3(SG:*Cmcm*).

Bond type	d^{μ} (Å)	v_b^{μ} (Å^3)	P	f_m ($\times 10^{-3}$)	H_v (GPa)
B-B	1.808	1.009	0.81	0	22.7
	1.816	1.023	0.77	0	
	1.845	1.072	0.75	0	
Nb-B	2.403	2.369	0.20	1.113	
	2.460	2.542	0.05	1.113	
	2.462	2.548	0.09	1.113	
	2.508	2.693	0.08	1.113	
	2.601	3.004	0.24	1.113	
Nb-Nb	2.951	4.388	0.04	1.113	

Table S10 Calculated bond parameters and Vickers hardness of Ti_2B_3(SG:*Cmcm*).

Bond type	d^{μ} (Å)	v_b^{μ} (Å^3)	P	f_m ($\times 10^{-3}$)	H_v (GPa)
B-B	1.753	0.842	0.90	0	28.9
	1.758	0.849	0.84	0	
	1.773	0.871	0.87	0	
Ti-B	2.352	2.032	0.20	1.368	
	2.382	2.111	0.04	1.368	
	2.386	2.122	0.06	1.368	
	2.393	2.141	0.09	1.368	
	2.425	2.228	0.06	1.368	
	2.520	2.500	0.24	1.368	
Ti-Ti	2.828	3.533	0.07	1.368	

Table S11 Calculated bond parameters and Vickers hardness of Mn_2B_3(SG:*C*2/*m*).

Bond type	d^{μ} (Å)	v_b^{μ} (Å^3)	P	f_m ($\times 10^{-3}$)	H_v (GPa)
B-B	1.714	1.444	0.82	0	20.9
	1.727	1.478	1.78	0	
	1.780	1.618	0.73	0	
	1.834	1.770	0.71	0	
	2.782	6.176	0.06	0	
Mn-B	2.073	2.555	0.22	3.458	
	2.162	2.899	0.12	3.458	
	2.168	2.923	0.23	3.458	
	2.190	3.013	0.48	3.458	
	2.192	3.021	0.12	3.458	
	2.195	3.034	0.29	3.458	
	2.203	3.067	0.12	3.458	
	2.246	3.25	0.02	3.458	
	2.428	4.106	0.24	3.458	

Table S12 Calculated bond parameters and Vickers hardness of Mn_2B_3(SG:*C*2/*c*).

Bond type	d^{μ} (Å)	v_b^{μ} (Å^3)	P	f_m ($\times 10^{-3}$)	H_v (GPa)
B-B	1.791	0.990	0.79	0	15.6
	1.854	1.099	0.69	0	
	1.938	1.255	0.57	0	
	2.232	1.917	0.04	0	
Mn-B	2.147	1.706	0.14	5.507	
	2.158	1.732	0.04	5.507	
	2.159	1.735	0.15	5.507	
	2.163	1.744	0.28	5.507	
	2.294	2.081	0.13	5.507	
	2.328	2.175	0.11	5.507	
	2.391	2.356	0.01	5.507	
Mn-Mn	2.565	2.909	0.01	5.507	

Table S13. The Bader charge analysis of five TM_2B_3s (TM = Mn, Cr, V, Nb and Ti), *C*2/*m*- and *C*2/*c*-Mn_2B_3 in 2×2×1 cells. The positive (negative) sign denotes the loss (gain) of electrons. There is the number of atoms in brackets.

	TM (e)	**B (e)**
Mn_2B_3	+0.55 (16), +0.78 (16)	-0.38 (8), -0.41 (8), -0.46 (16), -0.47 (16)
Cr_2B_3	+0.69 (16), +0.89 (16)	-0.45 (8), -0.49 (8), -0.51 (16), -0.59 (16)
V_2B_3	+1.12 (16), +0.87 (16)	-0.59 (8), -0.61 (16), -0.63 (8), -0.78 (16)
Nb_2B_3	+0.95 (16), +1.28 (16)	-0.61 (8), -0.63 (8), -0.74 (16), -0.88 (16)
Ti_2B_3	+1.04 (16), +1.29 (16)	-0.64 (4), -0.68 (20), -0. 66 (8), -0.99 (2), -1.00 (14),
***C*2/*m*-Mn_2B_3**	+0.53 (16), +0.78 (16)	-0.36 (8), -0.38 (8), -0.44 (8), -0.45 (24),
***C*2/*c*-Mn_2B_3**	+0.56 (32)	-0.16 (16), -0.48 (32)

Table S14. The averaged –ICOHP values (in eV/per bond) and bond lengths (Å) computed for some stronger TM-B and B-B bonds in five TM_2B_3s (TM = Mn, Cr, V, Nb and Ti), *C*2/*m*- and *C*2/*c*-Mn_2B_3.

	TM-B, B-B	bond length	-ICOHP
Mn_2B_3	Mn-B	2.185	1.282
		2.165	0.843
		2.121	0.782
	B-B	1.720	3.615
		1.717	3.525
		1.769	3.151
Cr_2B_3	Cr-B	2.262	2.185
		2.151	1.933
		2.117	1.769
	B-B	1.706	6.869
		1.732	6.735
		1.766	6.601
V_2B_3	V-B	2.318	2.198
		2.229	1.801
		2.212	1.518
	B-B	1.732	6.914
		1.725	6.867
		1.761	6.404
Nb_2B_3	Nb-B	2.403	2.193
		2.602	1.984
		2.379	1.925
	B-B	1.817	6.051
		1.809	5.901
		1.843	5.549

Ti_2B_3	Ti-B	2.510 2.353 2.341	1.862 1.590 1.256
	B-B	1.773 1.761 1.755	6.453 6.624 6.620
	Ti-Ti	2.819 2.991	0.772 0.295
*C*2/*m*-Mn_2B_3	Mn-B	2.175 2.179 2.111	1.234 0.919 0.830
	B-B	1.723 1.789 1.822	3.299 3.021 2.891
*C*2/*c*-Mn_2B_3	Mn-B	2.153 2.317 2.161	1.527 0.903 0.792
	B-B	1.822 1.838	2.983 2.702